Published in final edited form as:
Ultrasound Med Biol. 2016 December ; 42(12): 2893–2902. doi:10.1016/j.ultrasmedbio.2016.07.015.

Post-Procedure Evaluation of Microwave Ablations of Hepatocellular Carcinomas using Electrode Displacement Elastography

W. Yang[1], **T. Ziemlewicz**[2], **T. Varghese**[1,3], **M. Alexander**[2], **N. Rubert**[1], **A. Ingle**[3], **M. Lubner**[2], **J.L. Hinshaw**[2], **S. Wells**[2], **F.T. Lee Jr**[2], and **J.A. Zagzebski**[1]

[1]Department of Medical Physics, University of Wisconsin School of Medicine and Public Health, Madison, Wisconsin, 53706

[2]Department of Radiology, University of Wisconsin School of Medicine and Public Health, Madison, Wisconsin, 53706

[3]University of Wisconsin-Madison Department of Electrical and Computer Engineering, University of Wisconsin-Madison, Madison, Wisconsin, 53706

Abstract

Microwave ablation has been utilized clinically as an alternative to surgical resection. However, lack of real-time imaging to assess treated regions may compromise treatment outcomes. We previously introduced electrode displacement elastography (EDE) for strain imaging and verified its feasibility *in-vivo* on porcine animal models. In this study, we evaluated EDE on 44 patients diagnosed with hepatocellular carcinoma, treated using microwave ablation. The ablated region was identified on EDE images for 40 of the 44 patients. Ablation areas with EDE were 13.38 ± 4.99 cm^2, when compared to 7.61 ± 3.21 cm^2 on B-mode imaging. Contrast and contrast to noise ratios obtained with EDE was on the order of 232% and 98%, respectively, significantly higher than values measured from B mode images ($p < 0.001$). This study shows that EDE is feasible in patients and provides improved visualization of the ablation zone when compared with B-mode ultrasound.

Keywords

Ablation; Elastography; Elasticity Imaging; Microwave ablation; HCC; Strain imaging

Address all correspondence to: Tomy Varghese, Ph.D., Department of Medical Physics, University of Wisconsin School of Medicine and Public Health, University of Wisconsin-Madison, Madison, WI 53706, USA. **Voice:** (608)-265-8797, **Fax:** (608)-262-2413, tvarghese@wisc.edu.

Author Manuscript

Author Manuscript

Author Manuscript

Introduction

Hepatocellular carcinoma (HCC) is the 6th most common cancer and 3rd leading cause of cancer related mortality worldwide (Lencioni and Crocetti 2012). Surgical resection of liver tissue is the standard procedure for the cure of HCC although there are critical constraints for its wide-spread use. The following criteria have to be met for successful surgical resection: (1) the cancer is limited to a single liver lobe; (2) liver function is well preserved; and (3) the patient neither has abnormal bilirubin nor portal hypertension (Lencioni and Crocetti 2007). However, cirrhosis commonly occurs with HCC, and only up to 5% of cirrhotic patients with HCC fit the constraints described above for liver resection (Lencioni and Crocetti 2007). Therefore, as few as 9% of patients with HCC are suitable candidates for surgical resection (Liang and Wang 2007). With the development of minimally invasive treatments such as percutaneous radiofrequency ablation (RFA) and microwave ablation (MWA), thermal ablation has been adopted as the primary treatment option for HCC, especially for early stage interventions (tumor sizes < 3 cm) (Lencioni and Crocetti 2012; Shiina et al. 2012). Existing clinical studies have shown that treatment outcomes with ablation procedures are superior or at least equivalent to surgical resection or ethanol injection for these early stage HCC tumors (Lu et al. 2005; Lencioni and Crocetti 2007; Liang and Wang 2007; Lencioni and Crocetti 2012; Maluccio and Covey 2012; Shiina et al. 2012).

MWA, introduced as an ablation technique initially in Japan (Murakami et al. 1995), has now been increasingly applied worldwide (Shibata et al. 2002; Lu et al. 2005; Liang and Wang 2007; Maluccio and Covey 2012; Qian et al. 2012; Swan et al. 2013). Instead of generating the thermal dose by incorporating the patient as part of a closed loop circuit as in RFA, MWA emits microwave energy to agitate water molecules causing coagulation necrosis with a local impact. Thus, MWA delivers consistently higher intra-tumor temperatures, with reduced impact from blood flow in large vessels, enables faster ablation times, and provides an improved convection profile (Liang and Wang 2007; Lencioni and Crocetti 2012; Qian et al. 2012). Multiple probes can be applied simultaneously to create larger tumor ablation volumes (Harari et al. 2015). MWA therefore has several advantages over RFA including increased power, increased volume of direct heating, ablation consistency in different tissue types, and no requirement for ground pads (Lubner et al. 2013; Wells et al. 2015b; Ziemlewicz et al. 2016). With these technological advantages, MWA has been increasingly cited as the more commonly utilized percutaneous ablation method (Wells et al. 2015a; Ziemlewicz et al. 2015). Some investigators have reported that MWA does not show an obvious improvement over RFA in treatment outcomes (Shibata et al. 2002; Lu et al. 2005; Qian et al. 2012), however these studies utilized previous generation microwave technology. When evaluating current generation technology, MWA has shown a significantly lower rate of local tumor progression than RFA (Potretzke et al. 2016). The modality limitation might also be compensated by other treatment methods such as trans-arterial chemoembolization (TACE) to limit the blood supply from the hepatic artery to reduce the heat sink effect of large vessels (Liang and Wang 2007; Maluccio and Covey 2012). One recent study has shown that MWA could lead to satisfactory outcome even for tumor sizes greater than 3 cm which was previously considered to be the maximum suitable size for thermal ablation procedures (Ziemlewicz et al. 2015).

Ultrasound elastography has been considered as an alternative for ablation monitoring since the stiffness contrast between an ablated region and surrounding tissue is high (Righetti et al. 1999; Varghese et al. 2002; Varghese et al. 2003a; Bharat et al. 2005; Bharat et al. 2008b; Fahey et al. 2008; Kolokythas et al. 2008; Zhang et al. 2008; Rubert et al. 2010; Mariani et al. 2014; Zhou et al. 2014), and is not significantly impacted by the presence of gas bubbles (Varghese et al. 2004). Conventional, quasi-static ultrasound elastography is dependent on either an externally applied compression (Ophir et al. 1991) or internal physiological deformations (Varghese et al. 2003b; Varghese and Shi 2004; Shi and Varghese 2007) to produce displacements for estimating local tissue strain. The need for an external compressor would restrict the use of ultrasound elastography because it is cumbersome and generally cannot produce tissue displacements at sufficient depth. Acoustic radiation force (Sarvazyan et al. 1998; Nightingale et al. 2001; Fahey et al. 2008; Hoyt et al. 2008; Bing et al. 2011; Mariani et al. 2014), could be more suited for this task, but ARFI is limited by the small tissue displacements that can be generated (around 0.01 mm), and a relatively shallow imaging depth of around 8 cm. Beyond this depth the acoustic radiation force generated is too small to deform tissue due to attenuation of the signal (Zhao et al. 2011; Deng et al. 2015). The resulting data are also very sensitive to physiological motion such as cardiac pulsation and respiratory artifacts.

We previously introduced a novel, quasi-static ultrasound elastography technique, referred to as electrode displacement elastography (EDE) (Varghese et al. 2002; Bharat et al. 2008b; Rubert et al. 2010), designed specifically for monitoring percutaneous ablation procedures. Here the local tissue deformation for elastography is induced by manual perturbation of the ablation antenna (Varghese et al. 2002). In this study we investigated the feasibility of EDE in a clinical study done on 44 patients diagnosed with HCC and treated with MWA. The delineation of the ablated region on EDE images is compared with ablated region contours taken from conventional B mode images. Comparisons between the two modalities are made of the estimated ablation zone areas and of the detectability using contrast and contrast to noise ratio (CNR) features.

Materials and Methods

Patients and MWA system

Forty-four patients who underwent MWA for their HCC tumors were involved in this study. Informed consent to participate in this study was obtained prior to the ablation procedure under a protocol approved by the institutional review board (IRB) at the University of Wisconsin-Madison. Patients received MWA treatments under general anesthesia. Ultrasound radiofrequency data for EDE were acquired following antenna insertion, prior to onset of ablation, and immediately after the ablation procedure prior to the ablation antenna being removed from the insertion site. EDE images that exhibited clearly distinguishable ablation regions were obtained on 40 of the 44 patients. Four patients were excluded from analysis as the ablation zone could not be clearly delineated due to insufficient compression or excessive signal decorrelation artifacts.

MWA was delivered using a Neuwave Medical Certus 140 (Madison, WI, USA) operating at 2.45 GHz. Ablation duration and power were adjusted for each patient depending on the tumor size and location, with typical values of 5 min and 65 W, respectively. The MWA antenna was inserted under conventional ultrasound B mode imaging guidance in a CT imaging suite. In several patients multiple MWA antennae (maximum of 3, typically 2) were inserted at the same ablation site. MWA antenna position and placement within the ablation region were also confirmed using CT scans prior to the ablation procedure in cases where ultrasound B-mode imaging was not definitive. B-mode and EDE strain images were obtained after completion of the active ablation procedure, but prior to the complete dissipation of the gas bubbles to evaluate the post-treatment appearance.

EDE techniques and Strain image processing

The mechanical stimulus for EDE was induced by a physician by manually perturbing the ablation antenna. A small displacement (typically around 1 mm) was applied to the ablated region through the perturbation. No side effects such as additional bleeding or patient discomfort were noted as a result of the EDE procedure.

Loops of ultrasound radiofrequency data were recorded during the perturbation of the antenna. Data were acquired using a Siemens ACUSON S2000 system equipped with a curvilinear array transducer (6C1 HD) operating at a 4 MHz center frequency. Two frames of radiofrequency data were selected as “pre” and “post” deformation frames after reviewing the entire loop of images generated from the radiofrequency data. These data were then processed to estimate local tissue displacements. We selected frames such that the correlation coefficient between kernels did not drop below 0.75 at all depths to ensure that local displacements estimated are accurate (Chen and Varghese 2009). A two dimensional (2D) cross-correlation based tracking algorithm (Chen et al. 2009) was applied, where the cross-correlation kernel dimensions used were 3.5 wavelengths × 7 A lines. Assuming a sound speed of 1540 m/s and at a depth of 8 cm, the physical dimensions of the kernel were 1.35 mm × 3.29 mm along the axial and lateral direction, respectively. The kernel dimensions used are larger than those applied in breast elastography, where high frequency linear array transducers are used and kernel sizes of 0.385 mm (axial) × 0.507 mm (lateral) are applied (Xu et al. 2012). The larger kernel size was required in this study due to increased attenuation at deeper imaging locations, reducing the echo data signal-to-noise ratio, lower center frequency, and because of the smaller deformations introduced with EDE. Adjacent cross correlation kernels overlapped by 75% along the beam direction and one A-line in the lateral direction. Local displacement estimates were fit with a 15-point (0.375 μs, or 0.29 mm) linear, least squares fit, and the local strain values were computed as the gradient of the local displacements. EDE based strain images were generated offline on an Intel Core 2 Duo computer, with the tracking algorithm implemented using MATLAB (MathWorks, Inc. Natick, MA).

To account for the fan shaped geometry of data acquired using the curvilinear transducer, scan conversion was applied after displacement and strain estimations along the direction of the A-lines. A bi-linear interpolation was then applied to the strain values to calculate pixel values at scan converted positions on a rectangular grid.

Evaluation metrics for EDE vs. conventional B mode imaging

Area of the ablation region—Ablated zones are recognized in EDE because they exhibit lower strain than surrounding, untreated tissue. The estimated area of the ablation region was used as a feature to compare the 2D distribution of the low-strain zone on EDE and the hyperechoic region on B mode images. The ablation region was segmented manually on both sets of images. The area of the ablation region, S was calculated using:

$$S = \Delta \times N \quad (1)$$

where Δ is the image pixel size and N is the number of pixels inside the segmented region.

Ablation region contrast—The contrast of the ablation region is defined as:

$$C = \left| \frac{I_o - I_b}{I_o + I_b} \right| \quad (2)$$

where C represents the contrast, I_o is the mean image pixel value of a rectangular region of interest (ROI) positioned within the ablated region, and I_b is the mean pixel value of a similar sized rectangular ROI adjacent to the ablated region.

For EDE, the ROI of the ablated region was defined within the dark ellipse (see Fig 1 in Results, for example), which is the region with increased tissue stiffness. The background ROI was defined outside the bright halo around the ablated region. The upper limit of the strain values on the EDE images was set to a maximum of 0.025 or 2.5%, which was the approximate upper limit of the strain value introduced by the small needle perturbation. For B mode images, the ROI of the ablated region was defined within the bright gas bubble region, and the background ROI was selected from a region adjacent to the bubbles.

CNR of the ablation region—CNR, the contrast-to-noise ratio takes into consideration the noise level of the ablation region and background and is used to describe the detectability of the ablated region with the EDE strain image (Varghese and Ophir 1998). The CNR of the ablation region was calculated using:

$$CNR = 20 log_{10} \left(\frac{|I_o - I_b|}{\sqrt{\sigma_o^2 + \sigma_b^2}} \right) \quad (3)$$

where σ_o^2 and σ_b^2 represent the variance of the strain estimates within the ROI defined in the ablation region and background, respectively.

Measurement methods

Visualization and comparison of ablated regions on EDE strain and B mode images in this paper was not designed as a blinded study. A single observer with experience in *ex-vivo* and *in-vivo* MWA experiments delineated the ablated region area and selected the ROI for estimation of the contrast and CNR for both B mode and EDE strain images. B-mode images were analyzed before EDE strain images.

Statistical analysis

The area, contrast and CNR of the ablated region on EDE strain and B-mode images were compared pairwise for each patient studied. These were presented in the form of a scatter plot. Box and whisker plots were then used to perform a clustered comparison for the 40 patients, with the median value being the center bar within the box, the first and second quartile values denoted as the upper and lower borders of the box, and the 10^{th} and 90^{th} percentage values denoted by the top and bottom bar. The p value of the hypothesis that the values generated with EDE are greater than those with B mode images were calculated and represented with number of stars above the box and whisker plots.

Results

The high modulus contrast between the ablated region and the surrounding healthy tissue leads to a “saturated halo” appearance around the ablation zone on the EDE strain image, as shown in Fig. 1. Previous studies on TM phantoms and *in-vivo* porcine models have shown that the ablation zone on EDE matches histopathological ablation contours well in terms of target area and dimensions (Bharat et al. 2008b; Jiang et al. 2010; Rubert et al. 2010).

Figure 1, presents both the pre and post-ablation EDE strain and B-mode images for a patient with a 2 cm HCC diagnosed using pre-ablation magnetic resonance imaging. The liver was cirrhotic and the patient had not undergone any prior treatment for this tumor. HCC tumors are softer than normal liver tissue, and thus would be significantly softer than cirrhotic liver tissue (DeWall et al. 2012a). Note the clear visualization of two MWA antennae in the B-mode image obtained prior to the ablation, as two antennae were placed for this patient. The pre-ablation EDE strain image indicates the presence of a small stiffer region surrounding the ablation needle, due to the cyro-lock feature utilized to prevent needle movement following antenna placement, and an area of increased decorrelation at the location of the second antenna. MWA ablation was performed for 5 minutes at a 65 Watt power level in this patient. The post-ablation EDE image indicates the ablated region as an ellipsoidal region of increased stiffness (Bharat et al. 2005; Kiss et al. 2009) that incorporates the ablation region produced from both antennae. The needle track in the post-ablation images indicates the antenna that was perturbed to generate the EDE strain image in Figs. 1-3.

Ablation zones viewed on EDE were compared to those seen on conventional ultrasound B mode images in terms of ablation region area, contrast and CNR. The maximum dimension of the ablated region is outlined on Figs. 2 and 3, for both EDE and B-mode images, corresponding to the length of major axis of the low-strain region and the gas bubble cloud formed immediately after the ablation procedure. Note from Fig. 2, that the location of segment with the largest dimension in both images does not coincide, and this was the case with most of the ablations. Therefore, a more representative metric such as the ablation area and strain contrast was utilized in our analysis. Also observe in Fig. 3 that the gas bubble region does not coincide with the ablated region.

Figures 4-7, summarize the different features utilized to compare the performance of EDE based strain imaging versus conventional B-mode imaging for evaluating the ablation zone following completion of the procedure. Scatter plots present measurements from all 40 patients, with a horizontal line denoting the mean of the EDE and B-mode measurements respectively. For the box-and-whisker plots the dashed long horizontal bar in each data sets represents the median value, with the first and third quartiles defined by the box while the error bar represents the 10% and 90% values of the distribution of the measured feature values.

Ablation region area on EDE and B mode images

Figure 4(a), presents scatter plots comparing ablation areas estimated with EDE with areas of the hyperechoic regions on B-mode images. Each vertical pair of filled circles and triangles denotes values for EDE strain and B-mode respectively for the same patient. The average area of the ablation zone on EDE was 13.38 ± 4.99 (standard deviation) cm^2. As a comparison, the average area on B mode images for the same patient data set was 7.61 ± 3.21 (standard deviation) cm^2. A statistical comparison of the ablation area visualized on EDE strain with the area on B-mode imaging is illustrated in Fig. 4 (b).

Contrast of ablation region on EDE and B mode

In a similar manner, the distribution of the contrast obtained on the 40 patients is shown in Fig. 5(a). The mean value of the ablation zone contrast with EDE strain images was 0.73 ± 0.08 (standard deviation) while, the mean value of contrast on B mode images for the same patient data set was 0.22 ± 0.08 (standard deviation) as indicated by the horizontal lines in Fig. 5(a). The scatter plot for the contrast indicates a significant separation between the contrast estimated for EDE and the B-mode contrast of the ablated region. The distribution of contrast between the ablation area and background is shown in Fig. 5 (b). Strain imaging appears to provide a significant improvement in ablation region delineation based on the contrast ($p < 0.001$).

CNR of the ablated region on EDE and B mode images

Finally, the CNR distribution for both EDE strain and B-mode imaging is illustrated in Fig. 6(a). The average CNR of the ablation zone on EDE was 10.94 ± 2.45 dB (standard deviation), while the average CNR on B mode images was 5.52 ± 3.37 dB (standard deviation). Observe that the CNR is always positive with EDE, while the CNR obtained with B-mode imaging shows a few cases with extremely poor CNR leading to reduced detectability of the ablated region. The box-and-whisker plots for the CNR for EDE strain and B-mode imaging is shown in Fig. 6 (b).

A two-dimensional scatter plot depicting contrast versus the ablation area for each patient is shown in Fig. 7. Observe the separation between the B-mode estimates for the 40 patients from the EDE estimates, which exhibit a higher contrast and larger ablation areas.

Discussion

EDE was applied on patients undergoing MWA therapy as a potential modality to define the post-procedure zone of ablation in this study. Strain images obtained using EDE demonstrated improved ablation region delineation when compared to conventional B mode images in terms of ablation area, image contrast and CNR as shown in Figs. 4-7. In addition, an approach that vibrates the ablation needle to generate and image shear waves, termed electrode vibration elastography has also been developed (Bharat and Varghese 2010; DeWall and Varghese 2012; DeWall et al. 2012b; Ingle and Varghese 2014).

In conjunction with EDE, ultrasound could become an effective modality for complete monitoring of the ablation zone during MWA treatments. Although conventional B mode imaging is used routinely in the clinic for guidance in the ablation antenna/electrode placement and for monitoring outgassing, it does not clearly define the ablation zone at the completion of the procedure (Malone et al. 1994). Currently the most common method to monitor the ablation margin at the completion of the procedure is X-ray computed tomography (CT). Contrast CT, the current clinical standard for confirmation of the success of the procedure, provides ablation zone volume estimation and margin definition. However, CT may not be available during the procedure in many centers. This may necessitate a repeated ablation procedure and reinsertion of an antenna in the liver if the ablation zone does not adequately cover the targeted tumor and tissue margins. Ultrasound EDE is nonionizing, and thus can be performed without radiation exposure to either the patient or physician. The demographics of the patients involved in this study was 10 female and 34 male, ranging in age from 33 to 83, which is summarized in Table 1.

It is important when treating with RFA to limit variations in thermal dose within the ablation volume and to avoid delivery of an incomplete dose to tumors, including those that are adjacent to large vessels (Lencioni and Crocetti 2012). This limits the application of RFA to smaller tumors and ones away from large vessels (unless other precautions are taken). Large tumors and ones near large vessels show a decrease of up to 50% in terms of complete tumor necrosis (Lencioni and Crocetti 2012). An adequate ablation margin around the tumor region is a key factor for the success of percutaneous ablation treatments (Lencioni and Crocetti 2007; Lencioni and Crocetti 2012; Maluccio and Covey 2012). Various studies suggest that the margin should extend between 0.5 – 1.0 cm into the tumor free region (Lencioni and Crocetti 2007; Lencioni and Crocetti 2012; Maluccio and Covey 2012). Thus, an effective thermal ablation margin monitoring method is crucial to guarantee a successful clinical outcome. Immediately following ablation therapy, a hyperechoic area is observed on ultrasound B-mode images due to out-gassing of water vapor, which resolves within about 10 minutes after the procedure. The ablated region with MWA is slightly hyperechoic centrally and around the periphery and hypoechoic elsewhere (Wells et al. 2015b; Ziemlewicz et al. 2016). Contrast-enhanced ultrasound imaging has also been useful in delineating HCC tumors pre-ablation (Minami and Kudo 2011) and the coagulated region post-ablation (Clevert et al. 2012).

Even in cases where ablation area estimations on B mode images were relatively close to those obtained on EDE strain, estimations of ablated areas on B mode images was always smaller due to a shadowing effect, as seen in Fig. 3. In Fig. 3 (b) the gas bubbles tended to accumulate towards the top of the ablation zone and thus the lower boundary of the ablation zone was blurred due to the shadowing effect caused by increased attenuation from the gas bubbles. Thus it was difficult to visualize the thermal dose distribution on the bottom half of the ablated region on B mode images, and this increases the uncertainty for physicians to judge if an adequate ablation margin has been applied uniformly around the ablation zone. On the other hand, as shown in Fig 3 (a), the ablation zone could be clearly identified on EDE strain. Thus the thermal dose distribution along any direction can be easily observed.

Based on the estimated ablation areas, EDE strain images were not significantly affected by tumor depth as illustrated in Table 2. EDE provides delineation of the ablated region for treated HCC regions both at shallow depths and for deeper ablated tumor regions. This result is unlike that reported for elastographic imaging using acoustic radiation force, which is generally limited by ultrasonic attenuation to depths lower than 8 cm (Zhao et al. 2011; Deng et al. 2015).

The major limitation of this study was the lack of real-time EDE imaging feedback to the physicians. Image processing was performed offline on an Intel Core 2 desktop computer. The average processing time for each EDE strain image was approximately one minute. In order to obtain real time feedback, a higher performance system or more efficient programming techniques would be necessary. This lack of real-time feedback also potentially affected the success rate of EDE strain imaging. We performed EDE on 44 patients and obtained successful strain imaging results in terms of distinguishable ablation zones on 40 of the 44 patients. The success rate was 90.9%, which would have been considerably improved by the immediate feedback that real-time imaging would have provided to the physician (Hall et al. 2003). Real-time feedback would allow physicians to more easily standardize the applied deformation using the ablation antenna. Several vendors currently do provide such feedback on their commercial elastography software, and this aspect can be easily addressed for this clinical application (Hall et al. 2003).

A second limitation of the study is the lack of ultrasound or EDE based volume information on the ablated region. We have previously demonstrated that three-dimensional volume reconstruction of ablated regions using EDE can be obtained (Bharat et al. 2008a), however a viable method of obtaining three-dimensional imaging information clinically in patients is essential. This can be done either with two-dimensional ultrasound arrays or more efficient scanning approaches (Ingle and Varghese 2014).

Side effects of EDE

The magnitude of the perturbation applied to the ablation antenna is within 1-2 mm. During the deformation of surrounding tissue and the ablated region, no relative slip between the surrounding tissue and ablation antenna was observed with EDE prior to or after the MWA procedure. There were no obvious side effects with EDE since the positioning of the ablation antenna was not affected after data acquisition. Because of the small range of displacements introduced by the antenna, the ablation procedure is not adversely affected (Varghese et al. 2002; Kolokythas et al. 2008; Varghese 2009).

Conclusions

In this paper we demonstrate that EDE is feasible during MWA procedures of HCC tumors regardless of tumor depth. EDE strain images provide improved ablation region delineation compared to conventional B mode imaging. Further work needs to be performed to assess the accuracy of the ablation margin delineated by EDE and whether the entire tumor with sufficient surrounding normal tissue has been treated. Comparison of EDE results to a clinical gold standard such as contrast enhanced CT is therefore essential.

Acknowledgements

This study was funded by NIH grant 2R01 CA112192. We are grateful to Siemens Medical Solutions USA, Inc., for providing the S2000 Axius Direct Ultrasound Research Interface (URI) and Software licenses.

Funded by NIH grant 2R01 CA112192.

References

Bharat S, Fisher TG, Varghese T, Hall TJ, Jiang J, Madsen EL, Zagzebski JA, Lee FT Jr. Three-dimensional electrode displacement elastography using the Siemens C7F2 fourSight four-dimensional ultrasound transducer. Ultrasound Med Biol. 2008a; 34:1307–16. [PubMed: 18374467]

Bharat S, Techavipoo U, Kiss MZ, Liu W, Varghese T. Monitoring stiffness changes in lesions after radiofrequency ablation at different temperatures and durations of ablation. Ultrasound Med Biol. 2005; 31:415–22. [PubMed: 15749565]

Bharat S, Varghese T. Radiofrequency electrode vibration-induced shear wave imaging for tissue modulus estimation: A simulation study. The Journal of the Acoustical Society of America. 2010; 128:1582–5. [PubMed: 20968329]

Bharat S, Varghese T, Madsen EL, Zagzebski JA. Radio-frequency ablation electrode displacement elastography: a phantom study. Med Phys. 2008b; 35:2432–42. [PubMed: 18649476]

Bing KF, Rouze NC, Palmeri ML, Rotemberg VM, Nightingale KR. Combined ultrasonic thermal ablation with interleaved ARFI image monitoring using a single diagnostic curvilinear array: a feasibility study. Ultrasonic imaging. 2011; 33:217–32. [PubMed: 22518953]

Chen H, Varghese T. Multilevel hybrid 2D strain imaging algorithm for ultrasound sector/phased arrays. Med Phys. 2009; 36:2098–106. [PubMed: 19610299]

Chen L, Treece GM, Lindop JE, Gee AH, Prager RW. A quality-guided displacement tracking algorithm for ultrasonic elasticity imaging. Medical image analysis. 2009; 13:286–96. [PubMed: 19081285]

Clevert DA, Paprottka PM, Helck A, Reiser M, Trumm CG. Image fusion in the management of thermal tumor ablation of the liver. Clin Hemorheol Microcirc. 2012; 52:205–16. [PubMed: 22960300]

Deng Y, Palmeri ML, Rouze NC, Rosenzweig SJ, Abdelmalek MF, Nightingale KR. Analyzing the Impact of Increasing Mechanical Index and Energy Deposition on Shear Wave Speed Reconstruction in Human Liver. Ultrasound in medicine & biology. 2015

DeWall RJ, Bharat S, Varghese T, Hanson ME, Agni RM, Kliewer MA. Characterizing the compression-dependent viscoelastic properties of human hepatic pathologies using dynamic compression testing. Phys Med Biol. 2012a; 57:2273–86. [PubMed: 22459948]

DeWall RJ, Varghese T. Improving thermal ablation delineation with electrode vibration elastography using a bidirectional wave propagation assumption. IEEE Trans Ultrason Ferroelectr Freq Control. 2012; 59:168–73. [PubMed: 22293748]

DeWall RJ, Varghese T, Brace CL. Visualizing ex vivo radiofrequency and microwave ablation zones using electrode vibration elastography. Med Phys. 2012b; 39:6692–700. [PubMed: 23127063]

Fahey BJ, Nelson RC, Hsu SJ, Bradway DP, Dumont DM, Trahey GE. In vivo guidance and assessment of liver radio-frequency ablation with acoustic radiation force elastography. Ultrasound in medicine & biology. 2008; 34:1590–603. [PubMed: 18471954]

Hall TJ, Zhu Y, Spalding CS. In vivo real-time freehand palpation imaging. Ultrasound Med Biol. 2003; 29:427–35. [PubMed: 12706194]

Harari CM, Magagna M, Bedoya M, Lee FTJ, Lubner MG, Hinshaw JL, Ziemlewicz T, Brace CL. Microwave Ablation: Comparison of Simultaneous and Sequential Activation of Multiple Antennas in Liver Model Systems. Radiology. 2015 (in press).

Hoyt K, Castaneda B, Parker KJ. Two-dimensional sonoelastographic shear velocity imaging. Ultrasound in medicine & biology. 2008; 34:276–88. [PubMed: 17935863]

Ingle A, Varghese T. Three-dimensional sheaf of ultrasound planes reconstruction (SOUPR) of ablated volumes. IEEE Trans Med Imaging. 2014; 33:1677–88. [PubMed: 24808405]

Jiang J, Brace C, Andreano A, DeWall RJ, Rubert N, Fisher TG, Varghese T, Lee F Jr. Hall TJ. Ultrasound-based relative elastic modulus imaging for visualizing thermal ablation zones in a porcine model. Phys Med Biol. 2010; 55:2281–306. [PubMed: 20354279]

Kiss MZ, Daniels MJ, Varghese T. Investigation of temperature-dependent viscoelastic properties of thermal lesions in ex vivo animal liver tissue. J Biomech. 2009; 42:959–66. [PubMed: 19362313]

Kolokythas O, Gauthier T, Fernandez AT, Xie H, Timm BA, Cuevas C, Dighe MK, Mitsumori LM, Bruce MF, Herzka DA, Goswami GK, Andrews RT, Oas KM, Dubinsky TJ, Warren BH. Ultrasound-based elastography: a novel approach to assess radio frequency ablation of liver masses performed with expandable ablation probes: a feasibility study. Journal of ultrasound in medicine : official journal of the American Institute of Ultrasound in Medicine. 2008; 27:935–46. [PubMed: 18499853]

Lencioni R, Crocetti L. Radiofrequency ablation of liver cancer. Techniques in vascular and interventional radiology. 2007; 10:38–46. [PubMed: 17980317]

Lencioni R, Crocetti L. Local-regional treatment of hepatocellular carcinoma. Radiology. 2012; 262:43–58. [PubMed: 22190656]

Liang P, Wang Y. Microwave ablation of hepatocellular carcinoma. Oncology. 2007; 72(Suppl 1):124–31. [PubMed: 18087193]

Lu MD, Xu HX, Xie XY, Yin XY, Chen JW, Kuang M, Xu ZF, Liu GJ, Zheng YL. Percutaneous microwave and radiofrequency ablation for hepatocellular carcinoma: a retrospective comparative study. Journal of gastroenterology. 2005; 40:1054–60. [PubMed: 16322950]

Lubner MG, Brace CL, Ziemlewicz TJ, Hinshaw JL, Lee FT Jr. Microwave ablation of hepatic malignancy. Semin Intervent Radiol. 2013; 30:56–66. [PubMed: 24436518]

Malone DE, Lesiuk L, Brady AP, Wyman DR, Wilson BC. Hepatic interstitial laser photocoagulation: demonstration and possible clinical importance of intravascular gas. Radiology. 1994; 193:233–7. [PubMed: 8090897]

Maluccio M, Covey A. Recent progress in understanding, diagnosing, and treating hepatocellular carcinoma. CA: a cancer journal for clinicians. 2012; 62:394–9. [PubMed: 23070690]

Mariani A, Kwiecinski W, Pernot M, Balvay D, Tanter M, Clement O, Cuenod CA, Zinzindohoue F. Real time shear waves elastography monitoring of thermal ablation: in vivo evaluation in pig livers. The Journal of surgical research. 2014; 188:37–43. [PubMed: 24485877]

Minami Y, Kudo M. Review of dynamic contrast-enhanced ultrasound guidance in ablation therapy for hepatocellular carcinoma. World J Gastroenterol. 2011; 17:4952–9. [PubMed: 22174544]

Murakami R, Yoshimatsu S, Yamashita Y, Matsukawa T, Takahashi M, Sagara K. Treatment of hepatocellular carcinoma: value of percutaneous microwave coagulation. AJR American journal of roentgenology. 1995; 164:1159–64. [PubMed: 7717224]

Nightingale KR, Palmeri ML, Nightingale RW, Trahey GE. On the feasibility of remote palpation using acoustic radiation force. The Journal of the Acoustical Society of America. 2001; 110:625–34. [PubMed: 11508987]

Ophir J, Cespedes I, Ponnekanti H, Yazdi Y, Li X. Elastography: a quantitative method for imaging the elasticity of biological tissues. Ultrasonic imaging. 1991; 13:111–34. [PubMed: 1858217]

Potretzke TA, Ziemlewicz TJ, Hinshaw JL, Lubner MG, Wells SA, Brace CL, Agarwal P, Lee FTJ. Microwave versus Radiofrequency Ablation Treatment for Hepatocellular Carcinoma: A

Comparison of Efficacy at a Single Center. J Vasc Interv Radiol. 2016; 27:631–8. [PubMed: 27017124]

Qian GJ, Wang N, Shen Q, Sheng YH, Zhao JQ, Kuang M, Liu GJ, Wu MC. Efficacy of microwave versus radiofrequency ablation for treatment of small hepatocellular carcinoma: experimental and clinical studies. European radiology. 2012; 22:1983–90. [PubMed: 22544225]

Righetti R, Kallel F, Stafford RJ, Price RE, Krouskop TA, Hazle JD, Ophir J. Elastographic characterization of HIFU-induced lesions in canine livers. Ultrasound Med Biol. 1999; 25:1099–113. [PubMed: 10574342]

Rubert N, Bharat S, DeWall RJ, Andreano A, Brace C, Jiang J, Sampson L, Varghese T. Electrode displacement strain imaging of thermally-ablated liver tissue in an in vivo animal model. Med Phys. 2010; 37:1075–82. [PubMed: 20384243]

Sarvazyan AP, Rudenko OV, Swanson SD, Fowlkes JB, Emelianov SY. Shear wave elasticity imaging: a new ultrasonic technology of medical diagnostics. Ultrasound Med Biol. 1998; 24:1419–35. [PubMed: 10385964]

Shi H, Varghese T. Two-dimensional multi-level strain estimation for discontinuous tissue. Phys Med Biol. 2007; 52:389–401. [PubMed: 17202622]

Shibata T, Iimuro Y, Yamamoto Y, Maetani Y, Ametani F, Itoh K, Konishi J. Small hepatocellular carcinoma: comparison of radio-frequency ablation and percutaneous microwave coagulation therapy. Radiology. 2002; 223:331–7. [PubMed: 11997534]

Shiina S, Tateishi R, Arano T, Uchino K, Enooku K, Nakagawa H, Asaoka Y, Sato T, Masuzaki R, Kondo Y, Goto T, Yoshida H, Omata M, Koike K. Radiofrequency ablation for hepatocellular carcinoma: 10-year outcome and prognostic factors. The American journal of gastroenterology. 2012; 107:569–77. quiz 78. [PubMed: 22158026]

Swan RZ, Sindram D, Martinie JB, Iannitti DA. Operative microwave ablation for hepatocellular carcinoma: complications, recurrence, and long-term outcomes. Journal of gastrointestinal surgery : official journal of the Society for Surgery of the Alimentary Tract. 2013; 17:719–29. [PubMed: 23404173]

Varghese T. Quasi-Static Ultrasound Elastography. Ultrasound Clin. 2009; 4:323–38. [PubMed: 20798841]

Varghese T, Ophir J. An analysis of elastographic contrast-to-noise ratio. Ultrasound Med Biol. 1998; 24:915–24. [PubMed: 9740393]

Varghese T, Shi H. Elastographic imaging of thermal lesions in liver in-vivo using diaphragmatic stimuli. Ultrason Imaging. 2004; 26:18–28. [PubMed: 15134391]

Varghese T, Techavipoo U, Liu W, Zagzebski JA, Chen Q, Frank G, Lee FT Jr. Elastographic measurement of the area and volume of thermal lesions resulting from radiofrequency ablation: pathologic correlation. AJR Am J Roentgenol. 2003a; 181:701–7. [PubMed: 12933463]

Varghese T, Techavipoo U, Zagzebski JA, Lee FT Jr. Impact of gas bubbles generated during interstitial ablation on elastographic depiction of in vitro thermal lesions. J Ultrasound Med. 2004; 23:535–44. quiz 45-6. [PubMed: 15098873]

Varghese T, Zagzebski JA, Lee FT Jr. Elastographic imaging of thermal lesions in the liver in vivo following radiofrequency ablation: preliminary results. Ultrasound Med Biol. 2002; 28:1467–73. [PubMed: 12498942]

Varghese T, Zagzebski JA, Rahko P, Breburda CS. Ultrasonic imaging of myocardial strain using cardiac elastography. Ultrason Imaging. 2003b; 25:1–16. [PubMed: 12747424]

Wells SA, Hinshaw JL, Lubner MG, Ziemlewicz TJ, Brace CL, Lee FT Jr. Liver Ablation: Best Practice. Radiologic clinics of North America. 2015a; 53:933–71. [PubMed: 26321447]

Wells SA, Hinshaw JL, Lubner MG, Ziemlewicz TJ, Brace CL, Lee FTJ. Liver Ablation: Best Practice. Radiol Clin North Am. 2015b; 53:933–71. [PubMed: 26321447]

Xu H, Varghese T, Jiang J, Zagzebski JA. In vivo classification of breast masses using features derived from axial-strain and axial-shear images. Ultrason Imaging. 2012; 34:222–36. [PubMed: 23160475]

Zhang M, Castaneda B, Christensen J, Saad WE, Bylund K, Hoyt K, Strang JG, Rubens DJ, Parker KJ. Real-time sonoelastography of hepatic thermal lesions in a swine model. Medical physics. 2008; 35:4132–41. [PubMed: 18841866]

Zhao H, Song P, Urban MW, Kinnick RR, Yin M, Greenleaf JF, Chen S. Bias observed in time-of-flight shear wave speed measurements using radiation force of a focused ultrasound beam. Ultrasound in medicine & biology. 2011; 37:1884–92. [PubMed: 21924817]

Zhou Z, Wu W, Wu S, Xia J, Wang CY, Yang C, Lin CC, Tsui PH. A survey of ultrasound elastography approaches to percutaneous ablation monitoring. Proceedings of the Institution of Mechanical Engineers Part H, Journal of engineering in medicine. 2014; 228:1069–82.

Ziemlewicz TJ, Hinshaw JL, Lubner MG, Brace CL, Alexander ML, Agarwal P, Lee FT Jr. Percutaneous microwave ablation of hepatocellular carcinoma with a gas-cooled system: initial clinical results with 107 tumors. Journal of vascular and interventional radiology : JVIR. 2015; 26:62–8. [PubMed: 25446425]

Ziemlewicz TJ, Wells SA, Lubner MG, Brace CL, Hinshaw JL, Lee FTJ. Hepatic Tumor Ablation. Surg Clin North Am. 2016; 96:315–39. [PubMed: 27017867]

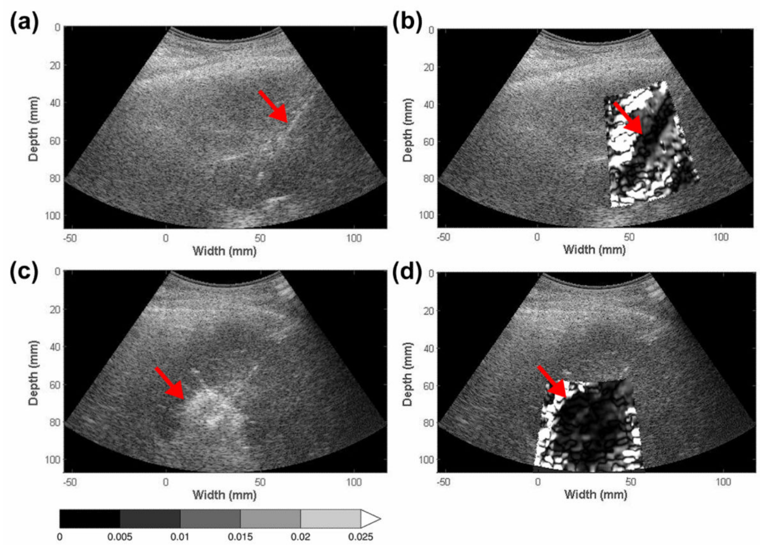

Figure 1.

Pre- and post- ablation regions depicted on EDE strain and corresponding B mode images for a patient diagnosed with a 2.0 cm HCC tumor. The targeted tumor region on B-mode (a) and EDE (b) are shown in the top row, while the ablated region on B-mode (c) and corresponding EDE strain (d) are shown in the bottom row. The ablation needle on the pre-treatment image (a) is identified by the echogenic line on the B mode image. EDE strain images were generated with a 3.5 wavelength × 7 A line cross-correlation kernel. The upper limit of the strain value was 2.5% and all values beyond were saturated as indicated by the colorbar.

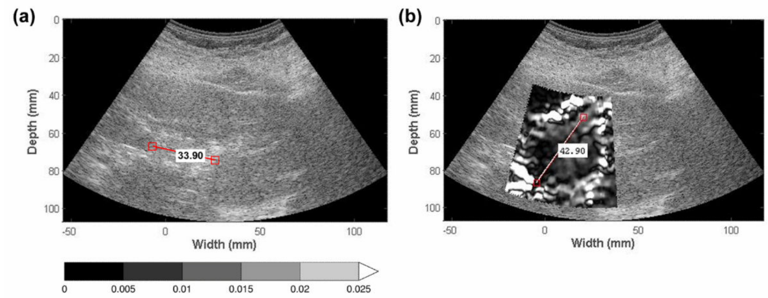

Figure 2.
Ablation region dimension measurement on EDE and B mode images. The maximum ablation region dimension on B mode (a) and EDE strain images (b) was measured. The gas bubble cloud on B mode images may be distorted leading to the maximum dimension being measured along different axes when compared to the EDE strain image as shown in (a) and (b).

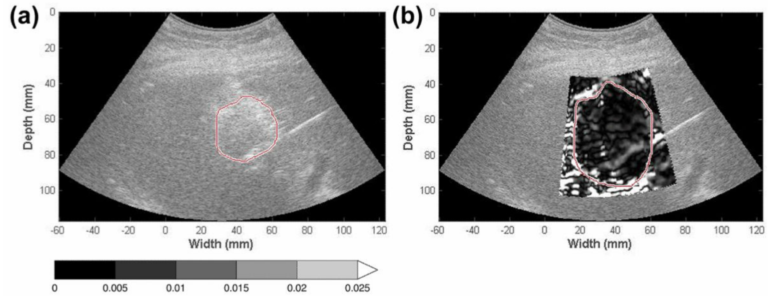

Figure 3.

Ablation area measurement on EDE and B mode images. The ablation region on B mode (a) and EDE images (b) was segmented manually with the segmented area calculated using Equation (1). The gas bubble cloud depicted as the hyperechoic region on B mode images (a) tended to accumulate at variable locations.

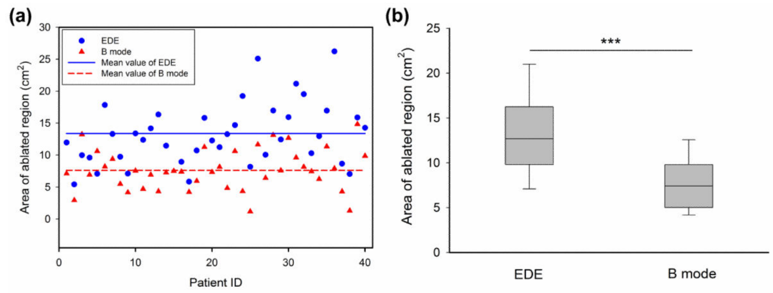

Figure 4.

Comparison of the ablation area measurements from B-mode (triangle) and EDE strain (circle) images, using scatter (a) and box and whisker plots (b). The mean value of the measurements is shown as the horizontal line in the scatter plot. For the box-and-whisker plot in (b), the dashed long horizontal bar in each data sets denotes the median value. The p value was <0.001 when comparing the mean values of EDE and corresponding B mode images, denoted by the three stars at the top.

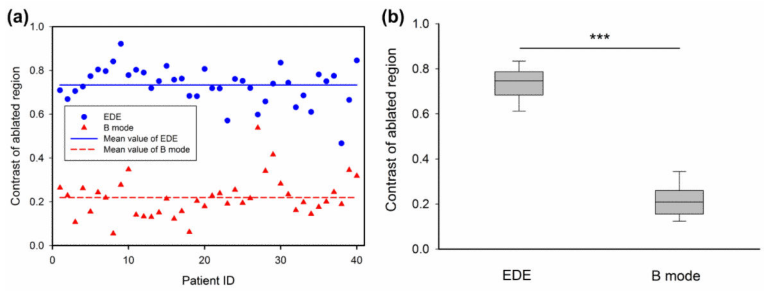

Figure 5.

Comparison of the ablation contrast measurements on B-mode (triangle) and EDE strain (circle) images, using scatter (a) and box and whisker plots (b).

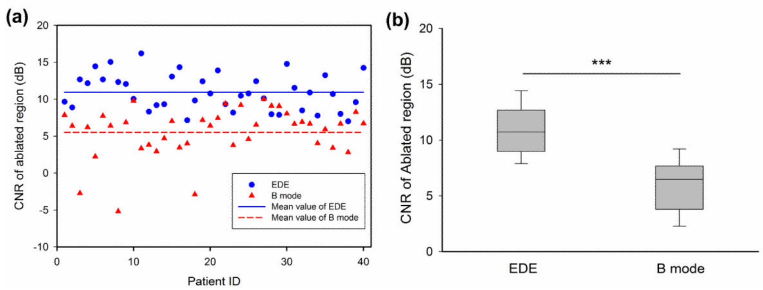

Figure 6.

Comparison of the CNR measurements on B-mode (triangle) and EDE strain (circle) images, using scatter (a) and box and whisker plots (b).

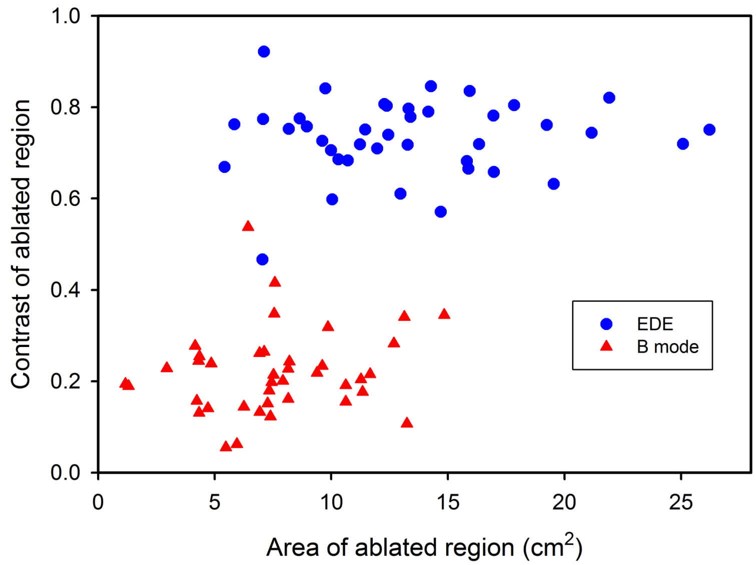

Figure 7.

Two-dimensional scatter plot showing ablation area versus contrast estimates for the ablated HCC tumors for B-mode (triangle) and EDE strain (circle). Observe the clustering of the B-mode and EDE data sets.

Table 1

Statistics of HCC patients reported in this study.

Patient features	**Value**
Age	64.4 ± 9.3 years
Gender (M/F)	34/10
Tumor size	2.2 ± 0.8 cm
Cirrhosis (Y/N)	37/7
Fatty Liver (Y/N)	1/43
Prior Treatment (Y/N)	10/34

Table 2

Details on HCC tumor depths and EDE imaging success on 44 patients.

HCC Depth	HCC Number	EDE Success	EDE Success Rate
< 5 cm	9	8/9	88.9%
> 5 cm < 8 cm	22	20/22	90.9%
> 8 cm < 10 cm	5	5/5	100%
> 10 cm < 15 cm	8	7/8	87.5%
Total	44	40/44	90.9%